A multiphase RANSE-based Computational Tool for the Analysis of Super-Cavitating Hydrofoils

Luca Bonfiglio
University of Genoa, Genoa, ITA
Visiting PhD student at Massachusetts Institute of Technology, Mechanical Engineering Department, Cambridge, Massachussets, USA

Abstract

Hydrofoils have been traditionally used in marine systems for propulsion and stabilization purposes. During 20th Century planning crafts started to be partially sustained by lift forces developed by immersed hydrofoils with the aim to decrease the wetted area, and hence the resistance. It is clear that hydrofoil design becomes a very important aspect for very high speed crafts. For this reason the flow have to be accurately solved to capture the complex hydrodynamic phenomena. A complete simulation framework consisting of an automatic grid generation module, a high fidelity CFD solver and a post-processing tool has been developed with the final goal to be included in a shape optimization process, specifically designed for cavitating or super-cavitating hydrofoils. The simulation framework has been coded to deal with any foil geometry with the minimum requirement of input data. The major complexities of hydrofoil fluid dynamic such as cavitation, laminar-turbulent transition, flow separation and vortex shedding are solved by a non-linear fully viscous method based on URANS equations, which has been carefully tuned for the solution of the flow around 2D foil geometries. The framework has been designed to post-process results which are given in terms of lift and drag coefficient. The grid strategy and the CFD solver setting have been specifically studied with the goal to obtain a relatively fast computational method which could still maintain high level of accuracy. The simulation framework has been validated with two different geometries at different angles of attack, tested at Caltech high-speed cavitation tunnel over a wide range of cavitation indexes. Interesting results are critically discussed involving fully cavitating flow over the entire hydrofoil (super-cavitating) and the unsteady behavior of the hydrofoil working at partially cavitating conditions. The multiphase flow is numerically solved considering water and vapor as a single fluid of characteristics that depend on an indicator scalar function as in the volume of fluid approach. Results have been verified on successively refined grid to understand the influence of mesh resolution on capturing the dynamic of the cavity. The main advantage of these methods is that there is no boundary condition on the cavity surface and the vapor flow is fully resolved allowing for a better solution of the pressure recovery at the cavity closure.

Key-words

CFD simulation framework; Hydrofoils; Super-Cavitating; RANSE; OpenFOAM

Nomenclature

α	Angle of attack
δ	Boundary layer thickness
γ	Volume of fluid scalar function
κ	Von Karman constant
μ,μ_L,μ_V	Dynamic viscosity of the fluid mixture, liquid, vapor
$\overline{v_t}$	Mean velocity parallel to the wall
ρ,ρ_L,ρ_V	Density of the fluid mixture, liquid, vapor
σ_K	cavitation index based on p_K
σ_V	cavitation index based on p_V
$\tau = \frac{TU}{c}$	Non-dimensional time parameter
$A = cs$	Reference hydrofoil area
BEM	Boundary Element Method
c	Hydrofoil chord
$c_D = \frac{D}{\frac{1}{2}\rho U^2 A}$	Drag coefficient
$c_L = \frac{L}{\frac{1}{2}\rho U^2 A}$	Lift coefficient
CFD	Computational Fluid Dynamic
f	Vortex shedding frequency
H	Height of the blunt trailing edge
n_0	Nuclei concentration per unit of volume
p_0	Reference atmospheric pressure
p_K	Pressure inside the cavity
p_V	Nominal saturation pressure
R	Bubble radius
$Re = \frac{\rho U c}{\mu}$	Reynolds number
s	Hydrofoil span
$Sr = \frac{fH}{U}$	Strouhal number
T	Overall simulation time
U	Inflow, free-stream velocity
u_τ	Shear velocity
$URANSE$	Unsteady Reynolds Averaged Navier Stokes Equations
VOF	Volume of fluid

$y+$ Dimensionless wall distance

Introduction and Background

The advances in high speed hydrofoil design have been brought to a larger audience in occasion of the recent America's Cup competition. Sailing hydrofoil boats have been able to reach speeds in excess of 40 knots with a simple concept: the wetted surface of the hull is minimized and the required displacement is obtained through a lifting force produced by submerged hydrofoils working close to cavitating condition. This is a well-known concept in naval architecture that has been exploited since the beginning of the 20th Century. The hydrofoils used in sailing boat races are yet not designed for cavitating flow, but if the speed will continue to increase, major changes in the design will be eventually needed. When very high speeds are essential, cavitation cannot be avoided and foil shapes have to be designed with the goal of maintaining a stable flow regime eventually compromising the lift. It is clear that a computational tool able to predict the hydrodynamic characteristics of cavitating foil is essential in the design process of such type of hydrofoils.
Super-cavitating flow conditions (i.e. the cavity is larger than the hydrofoil chord) have been studied and used to allow ultra high speed for the hydrofoil based crafts designed at the MIT-iShip Lab.
The numerical simulation of the flow around cavitating hydrofoils is a complex physical phenomenon which involves many different challenges. The early prediction methods were formulated under linear theories (Tulin (1953), Acosta (1955)) whose main weaknesses were in the cavity shape prediction especially for thick profiles. Uhlman (1987) used a non-linear surface vorticity method to prove that the cavity size decreases with the increase of profile thickness, in contrast with linear theories findings. Since then many non-linear potential flow based methods were formulated in the context of a boundary element approach both in 2D (Kinnas and Fine (1991)) and 3D (Fine and Kinnas (1993), Kinnas and Fine (1992) and Kim and Lee (1996)). Among these studies Young and Kinnas (2001) developed a surface panel method to predict cavitating flows in unsteady conditions.
The main problem related with cavitating flows is that the cavity shape can be found only through the solution of the flow around the profile which depend on the shape of the cavity itself. Panel methods treat the cavity as a domain boundary where specific dynamic and kinematic boundary conditions are imposed. They are based on potential flow formulation and they need to be formulated in order to iteratively solve for the cavity shape. Kinnas et al. (1994) developed a non-linear BEM for partially and super-cavitating hydrofoils including a viscous model based on the boundary layer-theory. The validity of this method has been proven for steady-state flows, but it cannot be applied for unsteady cavitation.
Recently a potential flow based method has been proposed by Celik et al. (2014) who used a BEM based on source and doublet distribution on the foil and the cavity with Dirichlet boundary conditions, validated with numerical results obtained with a Reynolds Averaged Navier-Stokes code. They investigated the steady sheet cavitation over NACA 16 hydrofoils, typically used in marine propeller design, applying an iterative method satisfying the dynamic boundary condition on the cavity and the kinematic one on the whole hydrofoil (including the cavity). Their method is limited to steady cavitaton occurring on the back of 2D profiles and its application to NACA 16 hydrofoils of different thickness, showed some weaknesses when used for thin profiles at different angles of attack. Their work confirms that in case of complex turbulent flows where hydrofoils are operated at high angles of attack a more realistic modeling of the physics need to be involved.
The solution of the Navier-Stokes equations coupled with a suitable cavitation model recently brought extraordinary improvements in cavitating flow predictions. Recovering viscous effects and vortex shedding due to separation in the context of a non-linear method to capture the cavity boundary has considerably improved the analysis of the unsteady characteristics of cavitation like the re-entrant jet prediction. However, one of the main challenges to face when solving Navier-Stokes equations in very high speed flows is the modeling of turbulent effects, responsible for the random fluctuations of the main flow variables. In fact the boundary layer flow interacts with the cavity interface, contributing to its development (Ji et al. (2015)). Many applications have been proposed for partially cavitating hydrofoils, but only few of theme consider super-cavitating conditions. In this paper we present a tool specifically designed for the analysis of marine hydrofoils: the open source libraries of OpenFOAM represent the core of a comprehensive fluid dynamic analysis tool which includes a pre-processing package for mesh generation, a 'case set-up' automatic procedure and a post-processing package for results analysis. This CFD suite is here used to study simple shaped super-cavitating foil geometries, with the goal to verify and validate the computational method based on Unsteady Reynolds Averaged Navier-Stokes Equations (URANS) which at the moment represents the best compromise between accuracy and computational effort. The present study represents a first step for the validation and verification of a cavitating solver meant to be included in the more general CFD analysis tool for hydrofoils.
The most distinguished feature of cavitating hydrofoils is the multiphase nature of the flow, which in this study is solved using a volume of fluid approach without involving any boundary condition on the cavity surface. In such a way the vapor flow is fully resolved allowing for a better solution of the pressure recovery at the cavity closure, both under partial and super-cavitating conditions

Methodology

Shape optimization is nowadays a well established practice in engineering design. Many successful applications have been presented in the past to demonstrate that designing the shape following intelligent optimization procedures leads to improve the hydrodynamic behavior of marine systems. These methods are

based on the geometry description through fully parametric models coupled with genetic algorithm driven by objective functions numerically defined by hydrodynamic solvers. A comprehensive application of this procedure as been given by Vernengo and Brizzolara (2015) who presented a multi-objective optimization of the shape of a multi-hull vessel around the hydrodynamic performances in calm water and rough sea.

Due to the large amount of design variables and consequent geometry variations, these methods need solvers able to perform complex numerical fluid dynamic predictions based on automatic procedures which minimize the computational effort. It is clear that potential flow solvers represent the vast majority of CFD methods applied to shape optimization problems.

Many concerns rise when the complexity of the hydrodynamic problem requires high level of accuracy in the flow field prediction. Campana et al. (2006) presented a Simulation Based Design environment for shape optimization specifically formulated to deal with highly expensive objective functions such as the one resulting from an high fidelity CFD solver as an URANSE code. Marine systems are mostly characterized by very complex hydrodynamic problems, for this reason shape optimization requires the improvement of both the optimization algorithms and the high fidelity solvers efficiency. The present study moves toward these goals through the development of a simulation framework specifically designed for the hydrodynamic analysis of cavitating and non-cavitating flows around any type of hydrofoil geometries under specific operative conditions.

Figure 1 presents the high level flow chart of the automatic procedure, implemented through a series of codes under Linux environment. First a mesh generation tool has to be designed and interfaced with an offset geometry output, then the CFD solver has to be set up according to the flow conditions. At last a post-processing tool is designed to extract CFD results in terms of hydrodynamic performances (lift and drag) and eventually cavity shape. The present work represents the key step toward the implementation of an efficient CFD solvers in a new shape optimization framework.

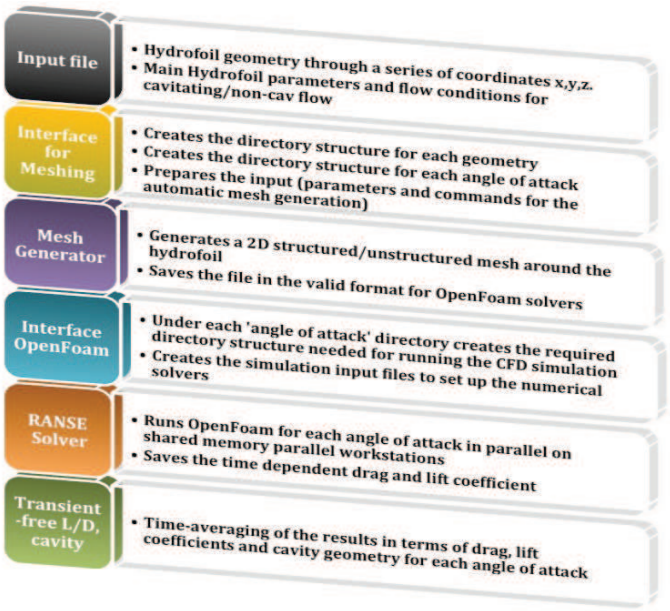

Figure 1: High Level Flow Chart of the Automatic Procedure for URANSE predictions of cavitating flows

Numerical Grid Generation

The definition of the computational domain represents the first step in modeling the problem of an unsteady viscous cavitating flow around a marine hydrofoil with the final goal of predicting the time-varying performances of the hydrofoil in terms of drag and lift forces as well as the cavity shape in terms of length and thickness. As previously discussed, high efficiency is required to implement a RANSE code into an optimization framework: unsteady simulations must be set up in order to reduce the computational time capturing the fundamental physical aspects of the problem when the transient-free stage is achieved. With this respect, one of the most important aspect is the determination of a suitable numerical grid able to predict viscous cavitating or non-cavitating flow eventually in presence of laminar-turbulent transition.

For this purpose a hybrid mesh composed by three different regions has been designed: a structured grid is used to discretize the region close to the hydrofoil surface while two unstructured grids are used for the near-body and the far flow fields. Boundary layer effects consequence of the non-slip condition lead to very high velocity and pressure gradients close to wall boundaries where a very high grid resolution is required to capture the effect of viscosity, vortex shedding and variable fluctuations due to turbulent effects. A structured grid helps reducing numerical errors due to sparse and irregular matrices and allows the control of the dimensionless wall distance $y+$, defined as:

$$y+ \equiv \frac{\rho u_\tau \delta s}{\mu} \tag{1}$$

This parameter is very important to set up the right boundary conditions at solid surface. As a matter of fact, it is well known that viscous effects are always present in the region where $y+ \leq 5-6$ which is also the so-called *viscous sub-layer* (Piquet, 1999). For high *Re* number convective effects are important only at $y \geq \delta$, where δ is the boundary layer thickness. It can be observed that for $y+ >> 1$ and $y/\delta << 1$ the mean velocity profile follows a logarithmic law:

$$u+ = \frac{\overline{v_t}}{u_\tau} = \frac{1}{\kappa} \ln y+ + B \tag{2}$$

Where $\overline{v_t}$ is the mean velocity parallel to the wall, $u_\tau = \sqrt{\frac{|\tau_W|}{\rho}}$ is the shear velocity (deriving from the shear stress τ_W, κ is the von Karman constant (0.41), B is an empirical constant related to the thickness of the viscous sublayer and y^+ is the non dimensional distance from the wall. Wall functions rely on the existence of this logarithmic region and they were introduced with the goal

to keep reasonable computational time in turbulent flows numerical simulations, exploiting the physical characteristics of wall bounded flows (Launder and Spalding (1972)). Kalitzin et al. (2005) Knopp et al. (2006) and Knopp (2006) presented some of the many successful applications of wall functions for the solution of the boundary layer of fully turbulent flow. In this cases relatively coarse grids with $y+$ greater than approximately 30 can be used for the solution of the flow in the logarithmic layer relying on different formulations for the solution in the viscous sublayer and the buffer layer (Launder and Spalding (1972)).
Bonfiglio and Brizzolara (2015) demonstrated that in case of transitional laminar/turbulent flow, wall functions do not allow for the prediction of the boundary layer physics, eventually leading to very inaccurate results. When the flow Re decreases eventually to fully laminar or transitional flow, the grid resolution close to the wall has to be increased in order to achieve very low $y+$ values thus resolving the flow characteristics up to the wall.
This physical considerations justify the needing of a flexible tool able to generate different structured grid close to the hydrofoil surface in order to simulate very different flow conditions. Moreover, in case of cavitating and super-cavitating flows, the presence of an interface region introduces a further intricacy in the mesh generation process, for this reason a near-body region outside the boundary layer is designed with the goal to increase the accuracy in cavity development prediction. This is the more refined of two nested unstructured regions discretized with tetrahedral elements distributed according to a Delaunay triangulation algorithm Delaunay (1934). Having two nested regions allows to decrease the number of cells in the far-field (outer unstructured region) without affecting the resolution of the cavity shape hence optimizing the global cells number.
The structured region close to the hydrofoil is bounded by two closed loops built around the foil profile: the first loop is obtained from the intersection between a transverse plane and the hydrofoil surface (*internal loop*), while the second (*external loop*) is an offset of the internal loop at a certain distance o. The region of fluid in between these loops is the one where viscous effects are more relevant, hence the o value is not given a priori, but it is an input parameter to be selected according to the particular flow condition (e.g. boundary layer thickness, presence of flow separation, recirculation or re-entrant jet, etc). Introducing a body-fitted curvilinear coordinate system ($\overline{n}$ and $\overline{t}$) and being d_1 the size of the first cell close to the wall in the direction normal to the surface ($\overline{n}$) and d_2 the size of the cell close to the external loop (farthest from the body in the structured region), it is possible to determine the number of cells and the progression in the $\overline{n}$ direction.

$$p_{\overline{n}} = \frac{o-d_1}{o-d_2} \qquad n_{\overline{n}} = \log_{p_{\overline{n}}} \frac{d_2}{d_1} + 1 \tag{3}$$

The cells size in $\overline{t}$ direction is related to the size in $\overline{n}$ direction (d_2) according to an aspect ratio factor AR to be tuned according to the particular flow conditions; no progression is used for distributing cells along the tangent direction. Describing the hydrofoil profile through a series of cubic splines of generic length l:

$$p_{\overline{t}} = 1 \qquad n_{\overline{t}} = \frac{l}{d_2 AR} \tag{4}$$

The surfaces used to mesh the structured region can be composed by several patches, one for each cubic spline used to model the hydrofoil profile. Each patch is bounded by the two cubic splines of the internal and the external loop and two straight lines perpendicular to the hydrofoil and connecting the ends of the inner and outer splines. The set of splines and straight lines is generated according to the requirements of a structured grid, hence a neighbor connectivity is maintained in the whole near-body region.
At first the hydrofoil geometry needs to be defined through input files containing the x, y and z coordinates of the points representing each wing section. Then the meshing tool reads coordinate files storing them in a primary set of points. These points are interpolated and a secondary set of points s generated with the goal to increase the accuracy in the geometry definition. The secondary set of points is used to define normal directions to the foil surface necessary to define the external outline bounding the fluid region adjacent to the hydrofoil geometry. A set of three normals (backward, forward and the sum of the previous two) can be associated to each primary point (Fig. 2). Defining the normal to the hydrofoil surface at the previous point (n_B) and the normal at the following point (n_F) the normal at the primary point can be obtained following equations (5), (6) and (7). The hydrofoil extrusion is defined moving each primary point of a quantity o in the normal direction n.

$$n_B = [\frac{(z_i - z_{i-1})}{\sqrt{(y_i - y_{i-1})^2 + (z_i - z_{i-1})^2}}; -\frac{(y_i - y_{i-1})}{\sqrt{(y_i - y_{i-1})^2 + (z_i - z_{i-1})^2}}] \tag{5}$$

$$n_F = [\frac{(z_{i+1} - z_i)}{\sqrt{(y_{i+1} - y_i)^2 + (z_{i+1} - z_i)^2}}; -\frac{(y_{i+1} - y_i)}{\sqrt{(y_{i+1} - y_i)^2 + (z_{i+1} - z_i)^2}}] \tag{6}$$

$$n = [\frac{n_{B1} + n_{F1}}{\sqrt{(n_{B1} + n_{F1})^2 + (n_{B2} + n_{F2})^2}}; \frac{n_{B2} + n_{F2}}{\sqrt{(n_{B1} + n_{F1})^2 + (n_{B2} + n_{F2})^2}}] \tag{7}$$

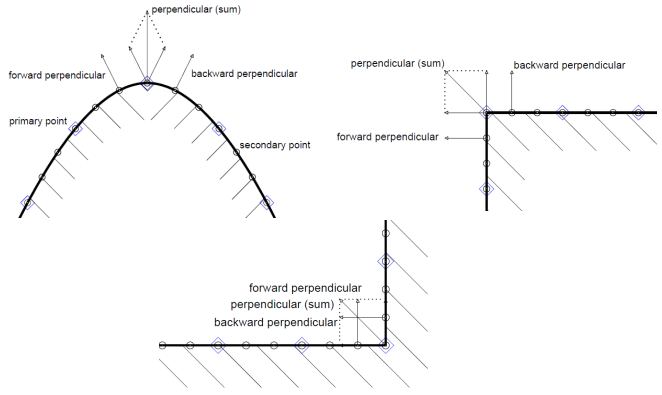

Figure 2: Normals in different geometries ("ordinary" - "convex" - "concave")

The ends of the cubic splines are indicated in the geomtery input file through a series of instructions defining three different types

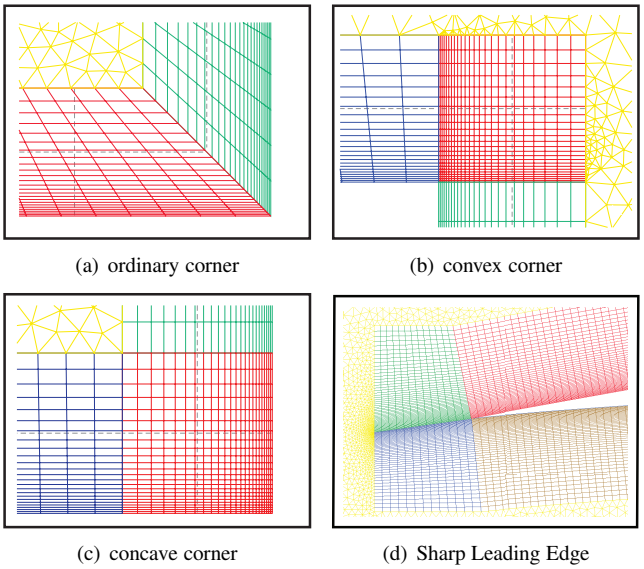

(a) ordinary corner (b) convex corner

(c) concave corner (d) Sharp Leading Edge

Figure 3: Grid definition for different geometries

of corners: *ordinary*, *convex* or *concave* (figure 3). A particular instruction is given in case of sharp leading or trailing edges, typical of supercavitating hydrofoil (*lecav*, *tecav*). If the ending point of a spline is *ordinary*, the primary point of the external loop will be obtained moving the corresponding internal point in the direction of n of a quantity o_o.

$$o_o = \frac{o}{\cos\frac{\theta}{2}} \tag{8}$$

Being θ the angle between n_B and n_F. If the corner is defined as *ordinary*, the mesh generated will be similar to the one showed in Fig. 3(a). Considering two adjacent cells, they will share a face: increasing angle θ leads to high skew angles between adjacent cells. To reduce the *skewness* keeping high mesh quality, in case where the hydrofoil profile curves in or out, the instructions *concave* or *convex* will launch two different routines to introduce additional patches between the two surfaces obtained from the two splines sharing one end (fig. 3(b) and fig. 3(d)). Following this procedure leads to the generation of a series of patches that are discretized using a structured algorithm.
Triangular elements are used to discretize the remaining surfaces, distributing the cells according to the cells size at the boundary points of the cavity-refinement region and the far-field. The size of the cells located at the computational domain boundaries is chosen as a multiple of d_3, the size of the remaining points is a consequence of the geometric distribution of cells in the structured mesh region.
The mesh generation is completed with the definition of the computational boundaries: *inlet*, *outlet*, *top*, *bottom* and *hydrofoil*.
The mesh generator tool performs the following steps (according to the flow chart in figure 1):

- Conversion of the input files (*hydrofoilGeometry.dat*) into a series of grid geometry instructions.
- Conversion of the grid geometry instructions into a *.msh* formatted file using an external meshing tool.
- Conversion of a *.msh* formatted grid into a grid suitable for RANSE solver. (*gmshToFoam* utility)
- Setting up of main folders where the simulation of the hydrofoil at different angles of attack is performed

The external meshing tool is GMSH, a three-dimensional grid generator able to deal both with structured and unstructured grid, developed by Geuzaine and Remacle (2009). The information required to perform the mesh generation are included in an input file described in table 1. Once input files are ready, the mesh generation is launched in bash and

Table 1: entries for the input file

1	Angle of attack to simulate (list ending with eao)	[deg]
noa	eao	[/]
1	Scale Factor	[/]
2	Offset (o)	[m]
3	Near wall cell size (d_1)	[m]
4	Size farthest cell from the wall (near-body region) (d_2)	[m]
5	Size farthest cell from the wall (d_3)	[m]
6	Cells Ratio	[/]
7	Reynolds number	[/]
8	Chord Length	[m]
9	Turb.Mod.: 0=lam./1=sa/2=kε /3=kωSST /4=kkl/5=rkε	[/]
10	Turbulent Intensity	[%]
11	Cavitation Parameter 0=nonCavitating 1=cavitating	[/]
12	Water Dynamic Viscosity	[kg/ms]
13	Water Density	[kg/m3]
14	Water Saturation Pressure	[Pa]
15	Reference Atmospheric Pressure	[Pa]
16	Vapor Dynamic Viscosity	[kg/ms]
17	Vapor Density	[kg/m3]
18	Simulation Time	[s]
19	Timing control for write output to file	[s]
20	Three dimensional extrusion	[m]
21	Number of CPUs for each Angle of Attack	[/]
22	0=SteadyState/1:Transient(laminar)/2:Transient(generic)	[/]
23	Transient-free simulation time	[s]
24	Free Stream=1/2=Cavitation Tunnel	[/]
25	Major Axis Ellipse/Length Tunnel	[m]
26	Minor Axis Ellipse/Depth Tunnel	[m]
27	Distance of the LE from the inlet of the domain	[m]
28	Initiall x of refinement region	[m]
29	Overall length refinement region	[m]
30	Overall breadth refinement region	[m]
31	Aspect Ration of cells in the prism layer	[/]
32	Wall Funtions: 1=yes 0=no	[/]

the numerical grids are stored in the respective simulation folders. Once the automatic generation of the mesh is performed it is possible to set up simulations according to the particular nature of the hydrodynamic problem.
Entry 1 in table 1 defines the list of angles of attack to be simulated. At the end of the list a code line indicating the end of the list is required (eao). From entry 2 to entry 6 a set of parameters governing cells dimension in the structured region as well as the cell distribution in the unstructured one are required. The maximum aspect ratio of the cells AR is defined in entry 31. Entry 27 represents the distance of the hydrofoil leading edge from the inlet, while entries 28,29 and 30 are used to place the cavity-shape refinement region in the computational domain. Two different domain shapes can be designed according to entry 24: an elliptical geometry is in fact preferred in case of a simulation of free-stream flow, while a rectangular shape can be chosen in case the numerical predictions have to be validated with cavitation tunnel experiments. The overall dimension of the computational domain are given in entries 24 and 25. The present automatic tool is specifically designed to be used in 2D simulations, but since OpenFOAM is intrinsically a 3D solver, an extrusion must be given in the direction perpendicular to the plane con-

taining the hydrofoil (entry 20).
Different turbulence models can be used in the numerical simulation (entry 9) and they can be eventually coupled with wall functions at solid boundaries (entry 32). The user can define the turbulence intensity level at the inlet (entry 10) and the flow *Re* (entry 7) as well as the nature of the hydrodynamic simulation: cavitating or non cavitating flow (entry 11) and steady or unsteady solution (entry 22).
From entry 12 to 17 the user has to specify the thermophysical characteristics of water and vapor in terms of density, dynamic viscosity, reference atmospheric pressure and water saturation pressure.
Simulation time can be controlled through entry 18 as well as the transient-free time necessary for the results post-processing (entry 23). The flow field output can be given with a time frequency different from the calculation time-step. In case where only the global results (lift and drag) are required, reducing the writing time-step is convenient for the overall computer usage both in terms of disk memory usage and of computational effort.
In the present paper the automatic procedure will be tested on two different hydrofoil shapes investigated by Parkin (1956). Very few 2D tests on super-cavitating hydrofoils are available in the open literature. The experimental results are compared with the numerical prediction of the cavitating flow around a flat plate (fig. 4(a)) and a circular arc (fig. 4(b)).

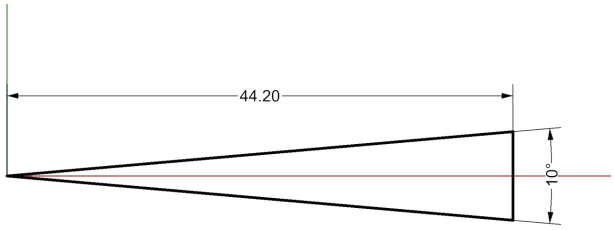

(a) Flat Plate Geometry

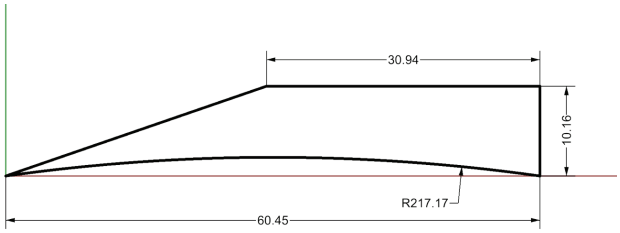

(b) Circular Arc Geometry

Figure 4: Parkin Geometries. Dimensions in *mm*.

Hydrofoils geometry and mesh topology

Geometries described in figure 4 are particularly interesting for the presence of sharp leading and trailing edges which enhance cavitation inception at relatively low speeds. Sharp edges are often used in cavitating hydrofoil design whenever predictable performances need to be ensured in a large range of operating conditions: the presence of a sharp edge causes a localized negative pressure peak which acts as a cavitator triggering the detachment of the cavity at the same point over a wide range of angles of attack and cavitation indexes (Brizzolara (2015)). In conventional super-cavitating hydrofoils they are typically present at the leading edge and at the two edges of the blunt trailing edge. The aim is to induce the detachment of the supercavity at the leading edge at low cavitation indexes and to induce separation and base cavitation at relatively high cavitation indexes or low angles of attack.
Both the flat plate and the circular arc geometries were experimentally tested at relative low Reynolds number. Parkin (1956) reported two different flow velocities (25 fps and 30 fps) without specifying which value was used for each run. In the present study results for 30 fps will be reported. Due to the small scale of the hydrofoils and the relatively low speed, a Reynolds number of $4.52e+05$ for the flat plate and of $6.19e+05$ for the circular arc lead to laminar flow regime over the entire hydrofoil wetted surfaces so no turbulence models were used in the numerical solution of the flow equation, i.e. the Navier-Stokes equations.
The size of the cell close to the wall in the direction normal to the surface is controlled by the parameter d_1/c and a geometric progression is used to distribute cells in the near-wall region according to the parameter d_1 and the size of the cell at the boundary of the structured region: d_2/c. The computational domain dimensions have been chosen to reproduce the cavitation tunnel used for the experiment at Caltech (Knapp et al. (1948)), thus having a length of 0.58 m and an height of 0.36 m. The leading edge is located at 0.265 m from the inlet and different angles of attack are simulated rotating the hydrofoil around the leading edge. Thetrahedral elements in the far field are distributed according to the size of the elements at the end of the major axis farthest from the hydrofoil d_3/c while the extension of the structured region is indicated through the parameter o/c.
The cell size close to the wall and the progression in the structured region (where a finer resolution is needed to accurately solve for the boundary or shear layers) have been systematically refined in order to obtain four different numerical grids characterized by decreasing $y+$ values as

Table 2: Flat Plate: parameters used to generate the FP series used in the mesh-sensitivity analysis at $\alpha = 0$ and cavitation index $\sigma_V = 0.141$.

Name	d_1/c	d_2/c	d_3/c	o/c	**Cells No**	**Est.** $y+$
FP1	1.35E-5	2.70E-4	4.73E-2	8.0E-4	30118	2.67
FP2	9.00E-6	1.80E-4	3.15E-2	8.0E-4	73002	1.78
FP3	6.00E-6	1.20E-4	2.10E-2	8.0E-4	154814	1.19
FP4	4.00E-6	8.00E-5	1.40E-2	8.0E-4	351908	0.86

Table 3: Circular Arc: parameters used to generate the FP series used in the mesh-sensitivity analysis at $\alpha = 0$ and cavitation index $\sigma_V = 0.277$.

Name	d_1/c	d_2/c	d_3/c	o/c	**Cells No**	**Est.** $y+$
FP1	1.35E-5	2.70E-4	4.73E-2	8.0E-4	37233	3.10
FP2	9.00E-6	1.80E-4	3.15E-2	8.0E-4	83698	2.06
FP3	6.00E-6	1.20E-4	2.10E-2	8.0E-4	189082	1.38
FP4	4.00E-6	8.00E-5	1.40E-2	8.0E-4	432930	0.92

shown in figures 5 and 6. Tables 2 and 3 presents the numerical values used for the mesh generation. Grids used in the present study are characterized by low values of $y+$, hence the laminar boundary layer is entirely solved up to the wall without the need for extrapolating functions (wall functions). Four snapshots in figures 5, 6 and 7 give a graphical representation of the numerical grids whose parameters are presented in tables 2 and 3. The refined region of unstructured elements aimed to increase the accuracy of the cavity interface production is evident in figure 5. Figure 6 shows a close-up of the structured elements around the sharp leading edge. The grids used for the circular arc geometry are presented in figure 7, where the near-body refinement regions are shown for the four sets of parameters in table 3.

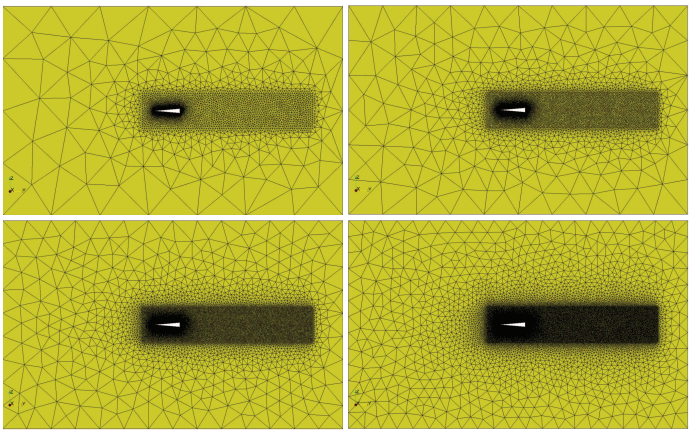

Figure 5: Numerical grids used in the sensitivity study. FP1 (top-left), FP2 (top-right), FP3 (bottom-left) and FP4 (bottom-right) (Table 2). Computational Domain

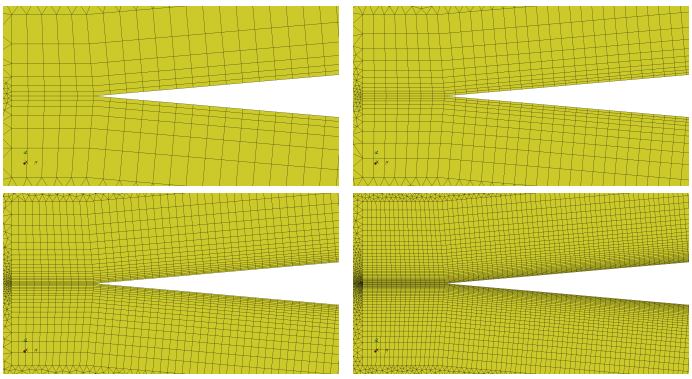

Figure 6: Numerical grids used in the sensitivity study. FP1 (top-left), FP2 (top-right), FP3 (bottom-left) and FP4 (bottom-right) (Table 2). Leading Edge

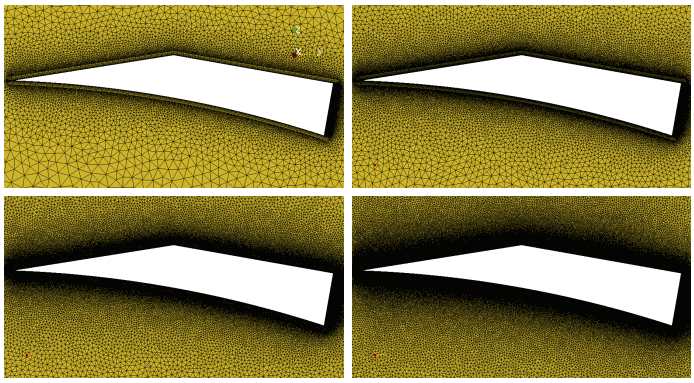

Figure 7: Numerical grids used in the sensitivity study. FP1 (top-left), FP2 (top-right), FP3 (bottom-left) and FP4 (bottom-right) (Table 3). Near-body region

Physical and Numerical Models

The prediction of the flow around an hydrofoil is here obtained through the numerical solution of the Navier-Stokes equations, which in a Cartesian reference frame are written as follows:

$$\frac{\partial(\rho u_i)}{\partial x_i} = 0 \tag{9}$$

$$\frac{\partial u_i}{\partial t} + \frac{\partial(u_i u_j)}{\partial x_j} = \frac{\partial}{\partial x_j}(\nu \frac{\partial u_i}{\partial x_j}) - \frac{1}{\rho}\frac{\partial p}{\partial x_i} + g_i \tag{10}$$

The system is a set of partial differential non linear equations in the unknows of pressure and velocity components. Modeling a cavitating flow implies the addition of a set of equations describing the thermophysical behavior of the fluid which can change its phase from liquid to vapor and vice-versa. Cavitation is a well-known phenomena and occurs in general in regions with high flow velocities where the pressure field drops below the vapor tension of the fluid at the local temperature.
Lord Rayleigh (1917) is considered the pioneer of the physical description of cavitation, his equations describe the dynamic of a spherical bubble with radius $R(t)$ in any point r of an incompressible, inviscid fluid giving an external pressure $P(t)$ and an internal pressure $p(R)$.

$$\dot{R} = \sqrt{\frac{3}{2}\frac{p(R) - P(t)}{\rho}} \tag{11}$$

The cavitation model used in the present study is the one proposed by Sauer and Scnherr (2001) which uses (11) to model the evolution of cavitation nuclei approximated to generic spherical bubbles of given diameter. In this study, the numerical solution of the flow governing equations is obtained using the open source libraries of OpenFOAM based on a finite volume approach with a collocated arrangement of variables. The unsteady cavitating viscous flow simulations are performed using *interPhaseChangeFoam*: a multiphase flow solver designed for two incompressible isothermal immiscible fluids with phase-change. This solver uses a volume of fluid phase-fraction based interface capturing approach. Hence momentum equations are solved for a single fluid mixture whose density and viscosity depend on the local concentration of vapor and water defined through the indicator function γ for which a transport equation is solved together with Navier-Stokes equations (OpenFOAM Foundation (2014)). The unsteady prediction of the cavity shape relies

on the accurate solution of the volume of fluid variable. A *compressive convection scheme* increases the accuracy of the interface prediction using an additional velocity field U_r to steepen the gradient of volume fraction function γ close to the cavity boundary. The conservation equation for γ is therefore written as:

$$\frac{\partial \gamma}{\partial t} + \nabla \cdot (\gamma U) + \nabla \cdot [\gamma(1-\gamma) U_r] = \frac{\dot{m}}{\rho_V} \tag{12}$$

Where the right hand side term represents a source term that will be discussed later in this section.
U_r represents the relative velocity between vapor and water: large values correspond to sharper interface but they might lead to numerical instabilities. In this approach the cavity surface is modeled as a fictitious interface where the VOF fraction γ assumes an intermediate value between 1 (liquid) and 0 (vapor): $\gamma = 0.5$. For this reason the numerical grid includes a refinement region of unstructured cells downstream the trailing edge where the cavity is supposed to develop. The solution of equation (12) leads to the determination of the physical characteristic of the fluid mixture:

$$\rho = (1-\gamma)\rho_L + \gamma \rho_V \tag{13}$$

$$\mu = (1-\gamma)\mu_L + \gamma \mu_V \tag{14}$$

The source term, rhs in (12) represents the vapor production, determined on the basis of equations that regulate the phase change of the fluid (vaporization and condensation):

$$\dot{m} = \begin{cases} \dot{m}^+ = C_V \frac{\rho_V \rho_L}{\rho} \gamma(1-\gamma) \frac{3}{R} \sqrt{\frac{2(p_V - p)}{3\rho_L}} & \text{if} \quad p < p_V \\ \dot{m}^- = C_C \frac{\rho_V \rho_L}{\rho} \gamma(1-\gamma) \frac{3}{R} \sqrt{\frac{2(p - p_V)}{3\rho_L}} & \text{if} \quad p > p_V \end{cases} \tag{15}$$

The bubble radius is given in terms of n_0 which represents the nuclei concentration per unit of volume of pure liquid:

$$R = \left(\frac{\gamma}{1-\gamma} \frac{3}{4\pi} \frac{1}{n_0} \right)^{\frac{1}{3}} \tag{16}$$

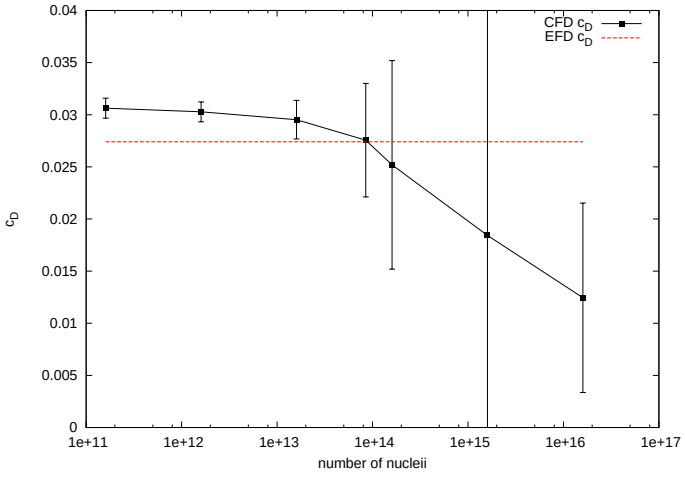

Figure 8: Shnerr Sauer model: Drag coefficient over nuclei concentration in 1 m^3 of water. Nuclei Diameter: $d_{nuc} = 2E-6$. $\sigma_v = 0.141, \alpha = 0\ deg, Re = 4.52e5$

A sensitivity study aimed to understand the influence of the nuclei concentration in the drag coefficient prediction has been performed and the results are presented in figure 8. A proper tuning of the cavitation model parameters may leads to a very close match between the numerical prediction and the experiments performed by Parkin (1956). The increase of nuclei concentration in the fluid leads to a larger vapor concentration at the hydrofoil surface which results in smaller time-averaged drag values. On the other hand, the larger number of cavitation nuclei increases the flow instabilities, leading to larger standard deviation values (indicated through the error bar in figure 8).
The numerical prediction of cavitating flows is achieved through the solution of the continuity and the momentum equations expressed in terms of a velocity and a pressure equation: the former solved using a *smoothSolver* with a Gauss Seidel smoother suitable for symmetric algebraic systems, while the latter using a multigrid method (*GAMG* - Geometric Algebraic Multi Grid) with a Diagonal Incomplete Cholesky based smoother. The outer iterations required for the solution of the non-linear partial differential system of equations rely on the PISO algorithm (Issa (1985)).
Being the nature of cavitation essentially unsteady, it is particularly important to accurately solve the problem in time domain. For this reason an *implicit Euler scheme* time discretization has been selected with a variable time-step calculated in order to keep the maximum local Courant number under a certain threshold ($Co < 1$). The solution of the volume of fluid fraction function is achieved using a *smoothSolver* with a Gauss Seidel smoother and a *Multidimensional Universal Limiter with Explicit Solution* (MULES) algorithm to avoid unbounded solution for the variable γ: if a cell is completely filled with a certain phase, it cannot be further filled with any other phases Kissling et al. (2010). The range of *Re* numbers investigated in the present study do not require any turbulence modeling.
The numerical set-up described above leads to the numerical solution of the pressure and velocity fields as well as the VOF scalar function.

Results

Different cavitating flow conditions can be distinguished through the definition of a nominal cavitation index σ_V (K_V), based on the fluid saturation pressure at ambient temperature and a cavitation index based on the actual pressure inside the cavity σ_K (K_K).

$$\sigma_V = \frac{p_0 - p_V}{\frac{1}{2}\rho V^2} \qquad \sigma_K = \frac{p_0 - p_K}{\frac{1}{2}\rho V^2} \tag{17}$$

The flat plate (or wedge) geometry has been investigated at two different angles of attack. Figure 9 shows results for the flat plate geometry at $\alpha = 0\ deg$ reported in terms of drag coefficient c_D versus cavitation index σ_V. A large range of σ_V was considered. The velocity and pressure field expressed in terms of the local cavitation index σ_K together with the cavity interface (boundary) line obtained for each simulation point are given in figures 11, 12, 13 and 14. For cavitation index $\sigma_V = 0.141$ and $\sigma_V = 0.608$ respectively. The variation of cavitation index σ_V has been obtained increasing the reference pressure p_0 at the given uniform inflow speed (30 ft/s).

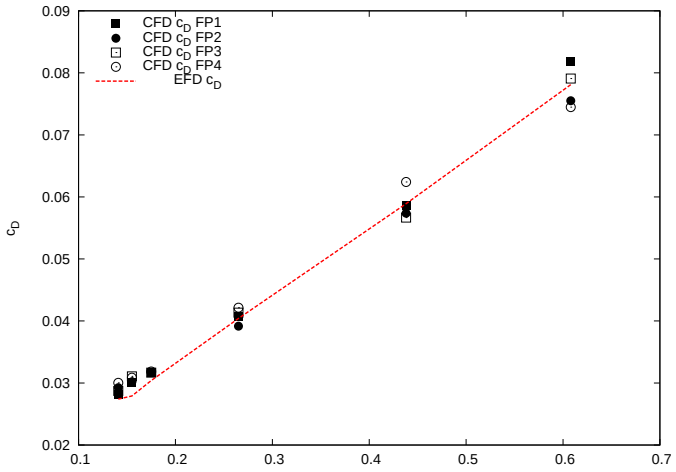

Figure 9: Drag Coefficient predictions at different cavitation indexes σ_v. Flat Plate geomtery at $Re = 4.52E5$, $\alpha = 0$ *deg*. Dots: numerical results obtained with different mesh resolutions; curve experimental measurements

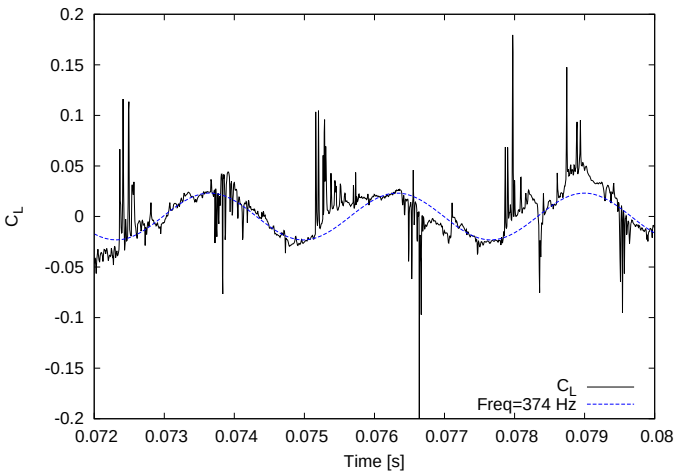

Figure 10: Lift Coefficient numerical predictions at $\sigma_v = 0.608$. Flat Plate geomtery at $Re = 4.52E5$, $\alpha = 0$ *deg* (black-continuous). Best-fit sinusoidal function of frequency $f = 374$ Hz

At this angle of attack ($\alpha = 0$ *deg*), the wedge is interested by base separation at high cavitation indexes and base cavitation at lower cavitation indexes. The cavity forms at the two sharp corners of the blunt trailing edge and it develops in the wake. The flow aft of the trailing edge and consequently the cavity is highly unsteady (particularly at the highest cavitation numbers), so the results are given in terms of averaged forces and snapshots of the flow field at different instants of time. Figure 9 demonstrates the very good agreement between the drag prediction obtained with the proposed numerical method.
The total simulation time has been chosen according to the non-dimensional parameter τ defined as:

$$\tau = \frac{TU}{c} \tag{18}$$

Where T is the total simulation time up to the measurement, U is the undisturbed flow velocity and c is the hydrofoil chord. The large value of non-dimensional simulation time ($\tau = 20.7$) has been selected with the aim to allow the whole development of the cavity length. The unsteady nature of cavitation does not allow to obtain a time-independent (steady state) result, for this reason a time-averaging process has been used over a non-dimensional time interval of $\tau = 6.2$. These time averaged forces are compared with the measured forces in cavitation tunnel. Even though no information about the experimental procedure of data analysis is reported by Parkin (1956), results in figure 9 are in accordance with experiments with a maximum error for the prediction at $\sigma_V = 0.155$ (7.6%) while in the remaining cavitation index range the error is below 5%. The standard deviation is higher at high cavitation indexes (26%) and it decreases for low σ_V. This confirms the unsteady nature of cavitating flow which directly corresponds to a fluctuation of the hydrodynamic forces. This phenomenon, in fact, increases at shorter cavity lengths, found at higher cavitation indexes. Figure 10 gives an example of the periodic fluctuation predicted for the lift component of the hydrofynamic forces around the zero mean, for the wedge hydrofoil at $\alpha = 0$ *deg*. The fluctuation corresponds to a periodic vortex shedding , as better discussed later on in this section.

Figure 11 presents some snapshots of the flow field predicted by the URANS model at the lowest cavitation index ($\sigma_V = 0.141$) in terms of velocity contour in the whole flow field. The vapor wake flow is stagnant right after the trailing edge where the flow detachment due to sharp edges create a recirculating region. The flow velocity inside the cavity increases getting closer to the cavity closure point. Far from the trailing edge the vapor and the liquid phase gradually reach the same velocity and no shear layer effects are present at the cavity interface. However in the closing region of the cavity the liquid phase flow closes quite sharply causing steep pressure recovery which in certain cases can lead to separation and vortex shedding. According the simple cavitation model implemented in the URANSE solver, which search for a sharp interface between the two phases, the cavity boundary effectively behaves like a rigid boundary up the the cavity trailing edge. In this region the vapor phase interacts with the liquid phase, partially mixing and dispersing and partially condensing (due to the high pressure peak).
The pressure recovery at the cavity trailing edge is clearly visible in figure 12 where the σ_K contour are plotted on top of the interface between the two phases: a very strong fluctuating pressure recovery region is experienced at the cavity closure. Figure 12 confirms that the cavitation model used in this study tends to impose a constant pressure inside the cavity equal to the saturated vapor tension. This is in disagreement with pressure values measured inside the cavity in the experiments which turned to be lower than the vapor tension.
When the reference ambient pressure is increased to reach higher cavitation index the length of the cavity reduces, as shown in figures 13 and 14. At $\sigma_V = 0.608$ a very short bubble is experienced at the trailing edge of the hydrofoil, drastically changing the flow field with respect to the lower cavitation indexes. Figure 13 shows the condition when the cavity closes right after the hydrofoil trailing edge, where very short cavity with a stagnant vapor flow still exists. First stages of bubble development (top-left panel in figure 14) are still characterized by a pressure recovery downstream the cavity, but after this initial transient state, a vortex shedding similar to the one due to flow aft of bluff bodies is experienced. The Von Karman vortex street is a consequence of the particular shape of this hydrofoil which clearly enhances separation at fixing points. The shedding frequency is usually reported in terms of Strouhal

number, defined as:

$$Sr = \frac{fH}{U} \tag{19}$$

Where f is the shedding frequency, H is the characteristic length (trailing edge height in this case) and U the free-stream velocity. The vorticity shed strongly depends on the free-stream velocity: increasing Re number generally leads (for similar flow patterns) to higher Sr. Being β the apex angle of the hydrofoil, experiments on wedge sections have been performed by Sjunnesson et al. (1991) on a $\beta = 60\ deg$ wedge at $Re = 4.5E4$ and resulting in $Sr = 0.25$. The unsteady cavitating flow past the $\beta = 10\ deg$ wedge predicted in the present study showed a vortex shedding characterized by a $Sr = 0.319$, higher than the one measured by Sjunnesson et al. (1991). The difference is due to the presence of the cavity and to the higher Re, both having the effect of enlarging the recirculation zone hence increasing the Sr.

Figures 15 and 16 present the validation of the predicted drag and lift forces for the flat plate (wedge) inclined at an angle of attack of 7 deg (face line to undisturbed inflow). The four different mesh resolutions presented in table 2 have been used to verify the numerical model over different flow conditions. The numerical simulation settings presented in the previous sections lead to very accurate prediction for the drag coefficient as shown in 15. The relative error with respect to experiments is generally below 5% being slightly larger for higher cavitation indexes. The average error in the whole σ_V range is 1.6% for mesh setting FP1, 3.1% for FP2, 2.8% for FP3 and 3.5% for FP4. An increase in mesh resolution does not show a clear trend in terms of error reduction, while it surely implies higher computational times. This confirms the robustness of the grid strategy.

While the drag coefficient seems to be accurately predicted in the whole σ_V range, the lift coefficient shows larger discrepancies with respect to experimental results, especially at higher cavitation indexes. The relative error for the coarsest grid is always below 10%, having an average value of 6.8% and generally increasing for higher cavitation index. More refined grids generally improve the lift coefficient prediction: 6.02% for mesh setting FP2, 5.0% for FP3 and 5.0% for FP4. It has to be observed that when the cavitation index increases, the cavity length reduces creating a recirculation region close to the hydrofoil trailing edge which results in a Von-Karman vortex shedding similar to the one in figure 14. As it is evidenced by the high values of standard deviation in figure 16, vortex shedding is responsible for the oscillation of forces on the hydrofoil surface.

Figure 17 presents a comparison between the cavity shape predicted by the proposed numerical method and that captured during the experiments, for the wedge profile at $\alpha = 7\ deg$. A series of 5 microseconds exposure time photographs of the experiments are available at several cavitation indexes, showing the instantaneous structure of the cavity and the wake behind the cavity.

These pictures are visually compared with the URANS results given in terms of VOF contours at $\tau = 20.68$ (red color indicating vapor and blue liquid). The flow condition at $\sigma_V = 0.191$ is presented in figure 17(a): a supercavity detaches from the leading edge and cover the whole hydrofoil surface, extending far from the blunt trailing edge. The total length of the cavity cannot be compared for this particular σ_V, but the cavity thickness on the hydrofoil surface predicted with the URANS solver generally is well in agreement with the experiments.

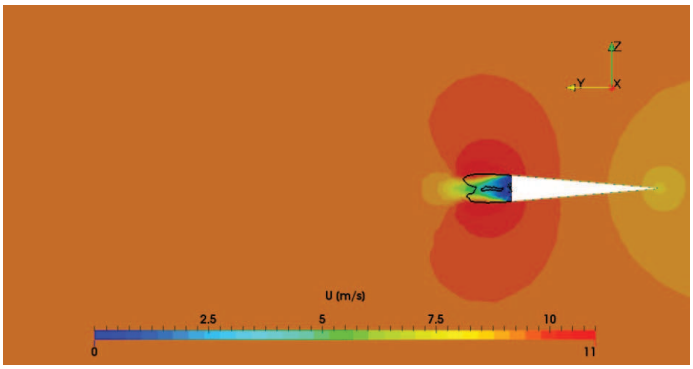

(a) $\tau = 0.41$

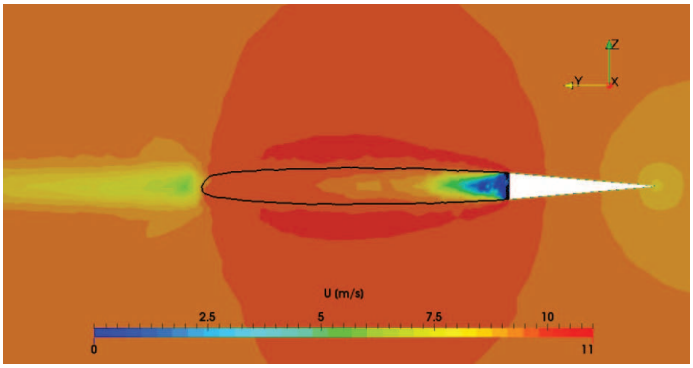

(b) $\tau = 4.13$

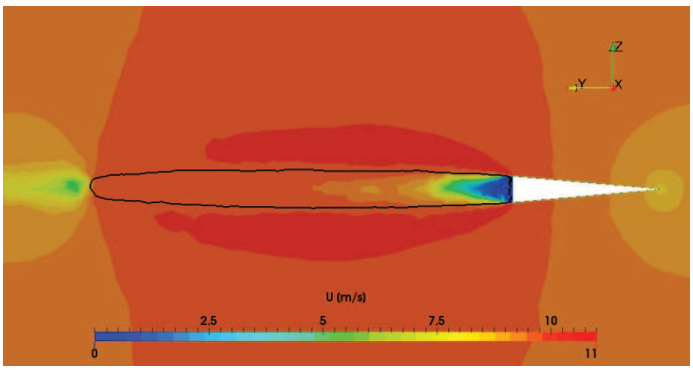

(c) $\tau = 10.35$

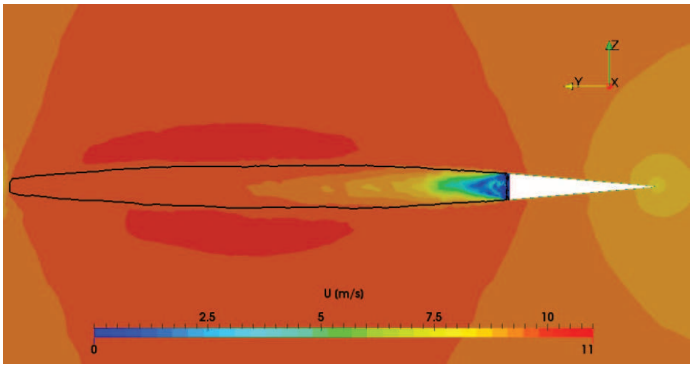

(d) $\tau = 20.69$

Figure 11: Unsteady flow solution: velocity Contours at cavitation index $\sigma_V = 0.141$ at different non-dimensional time instants $/tau$. Last time step corresponds to the steady state solution. In black $VoF = 0.5$

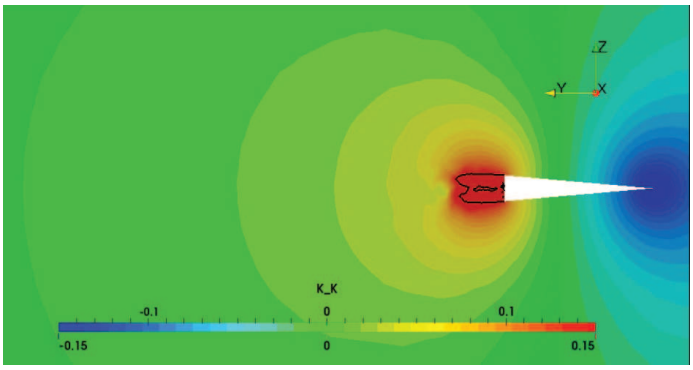

(a) $\tau = 0.41$

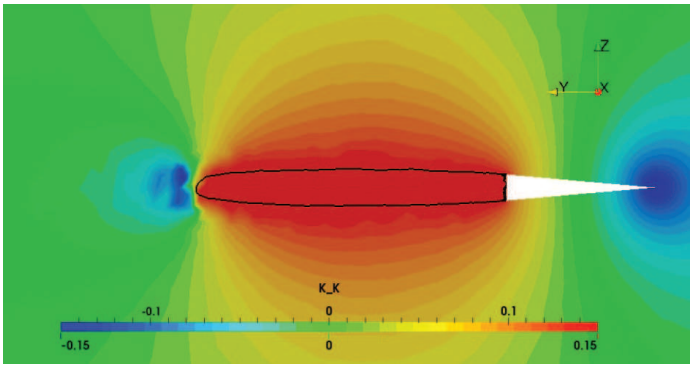

(b) $\tau = 4.13$

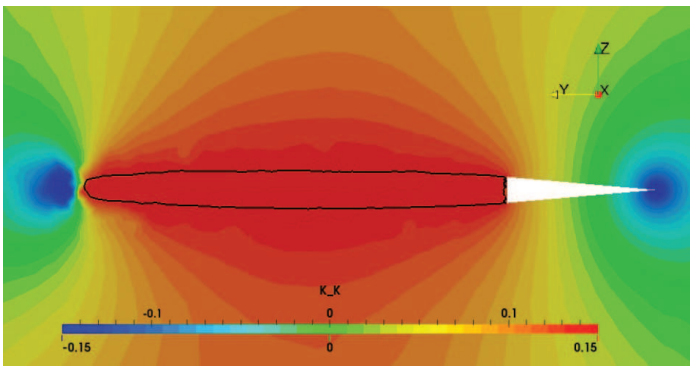

(c) $\tau = 10.35$

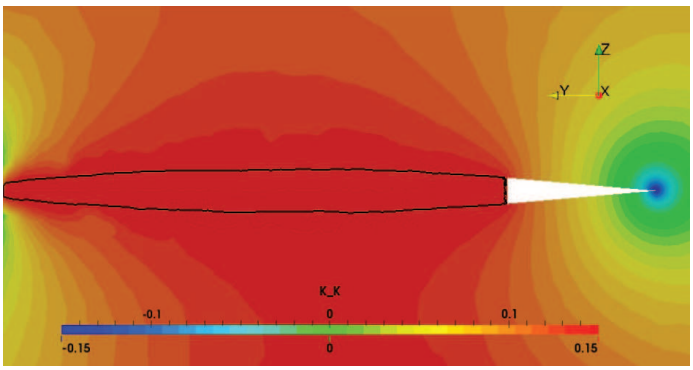

(d) $\tau = 20.69$

Figure 12: Unsteady flow solution: σ_K Contours at cavitation index $\sigma_V = 0.141$ at different non-dimensional time instants $/tau$. Last time step corresponds to the steady state solution. In black $VoF = 0.5$

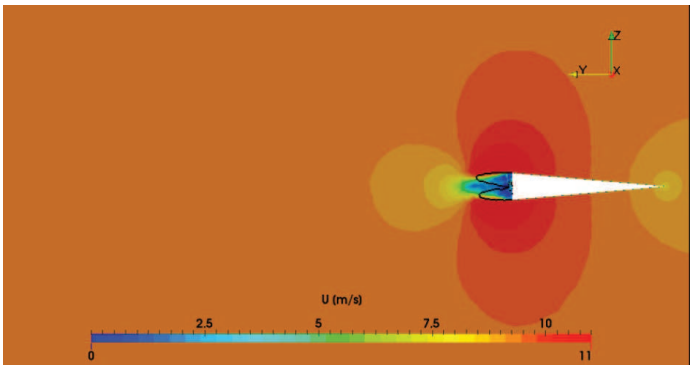

(a) $\tau = 0.41$

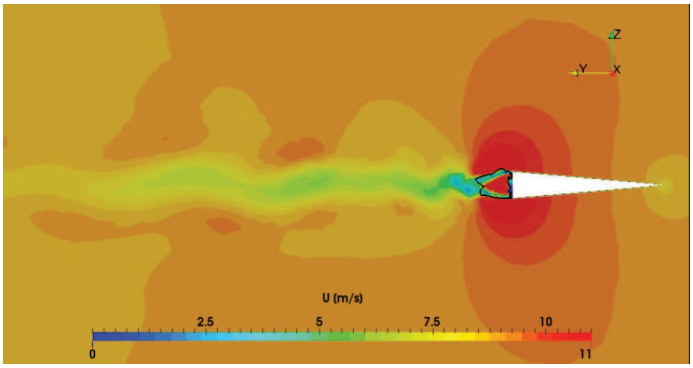

(b) $\tau = 4.13$

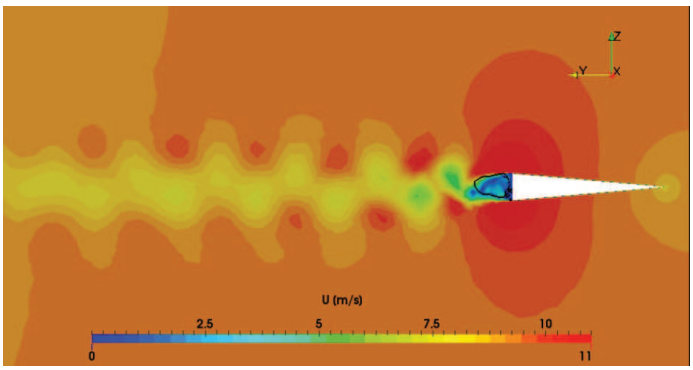

(c) $\tau = 10.35$

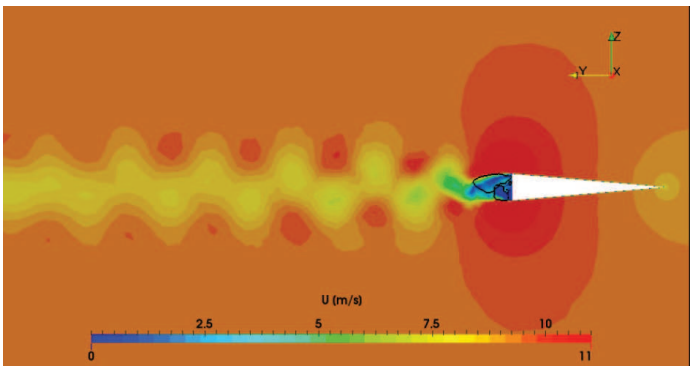

(d) $\tau = 20.69$

Figure 13: Unsteady flow solution: velocity Contours at cavitation index $\sigma_V = 0.608$ at different non-dimensional time instants $/tau$. Last time step corresponds to the steady state solution. In black $VoF = 0.5$

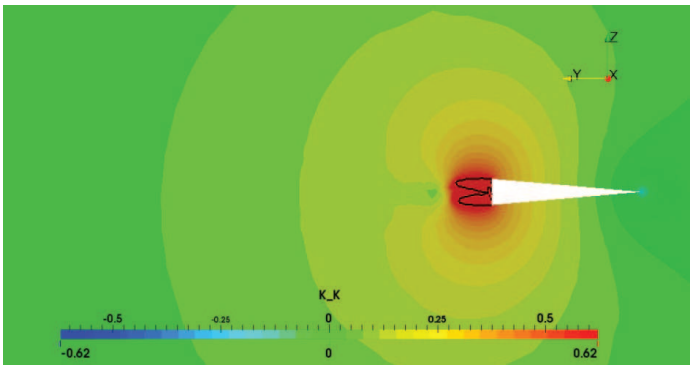

(a) $\tau = 0.41$

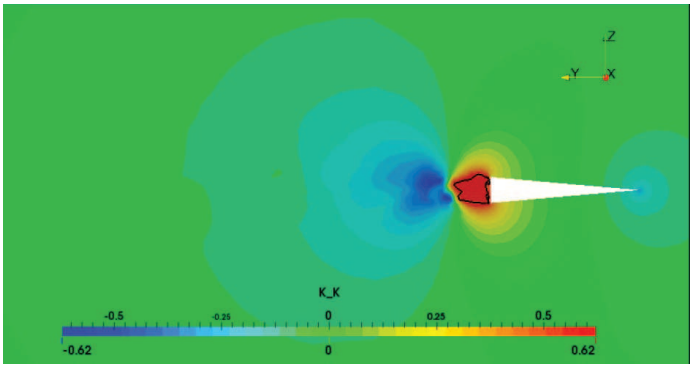

(b) $\tau = 4.13$

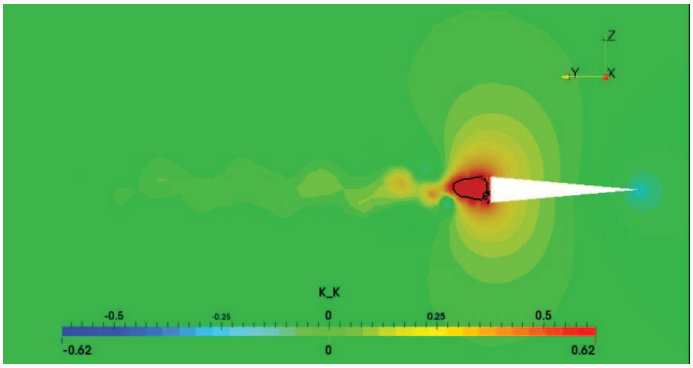

(c) $\tau = 10.35$

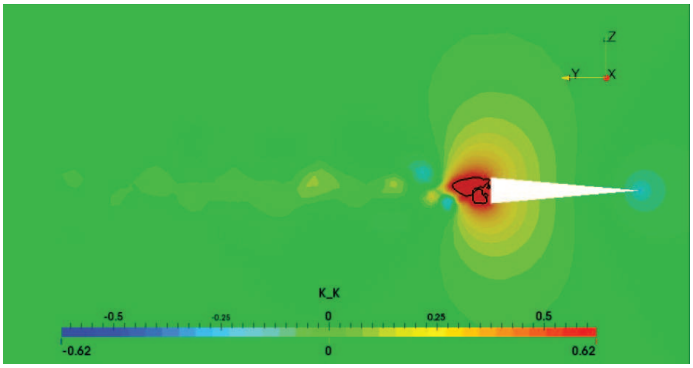

(d) $\tau = 20.69$

Figure 14: Unsteady flow solution: σ_K Contours at cavitation index $\sigma_V = 0.608$ at different non-dimensional time instants $/tau$. Last time step corresponds to the steady state solution. In black $VoF = 0.5$

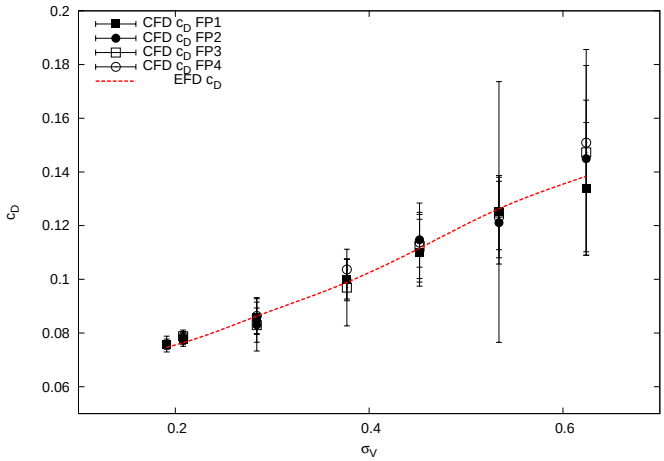

Figure 15: Drag Coefficient predictions at different cavitation indexes σ_v. Dots: numerical results obtained with different mesh resolutions; curve experimental measurements. Flat Plate geomtery at $Re = 4.52E5$, $\alpha = 7$ *deg*.

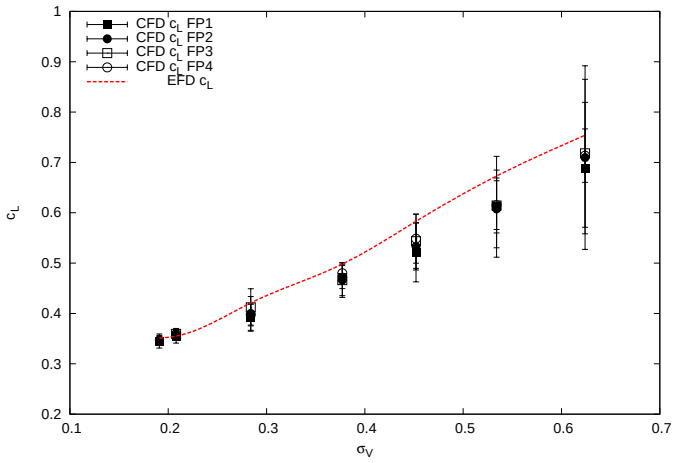

Figure 16: Lift Coefficient predictions at different cavitation indexes σ_v. Dots: numerical results obtained with different mesh resolutions; curve experimental measurements. Flat Plate geomtery at $Re = 4.52E5$, $\alpha = 7$ *deg*.

An increase of σ_V results in a reduction of the cavity length and thickness as confirmed by figure 17(b), which presents results for $\sigma_V = 0.284$. The cavity length predicted by the CFD method perfectly matches the experiments. A good agreement is found also in the cavity thickness, both on the hydrofoil surface and in the wake region.
The wake instability starts to occur at higher cavitation indexes: in figure 17(c), results for $\sigma_V = 0.534$ clearly show a very short cavity length that in this flow condition closes at about $0.5c$ aft of the trailing edge. Cavities shorter than half a cord are known to be unstable (Acosta (1955)). Also in this case an almost perfect agreement between the predicted and the measured shape has been found.
Figures 18 and 19 present results obtained for the circular arc at $\alpha = 0$ *deg*. Also in this case, the four different grids presented in table 3 have

been used in the whole σ_V range. Global results in terms of drag coefficient are reported in figure 18.

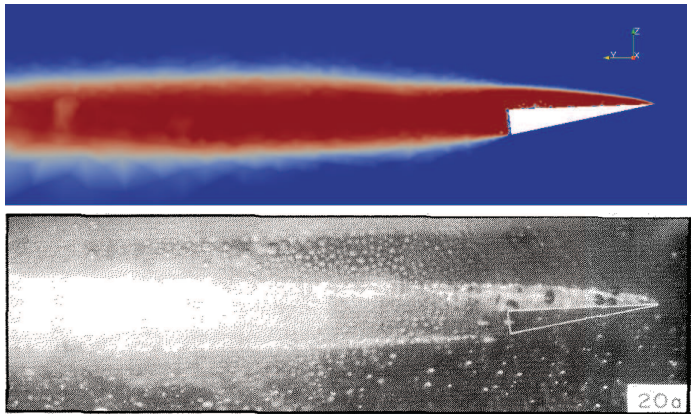

(a) $\sigma_V = 0.191$ Top pannel CFD, bottom pannel EFD

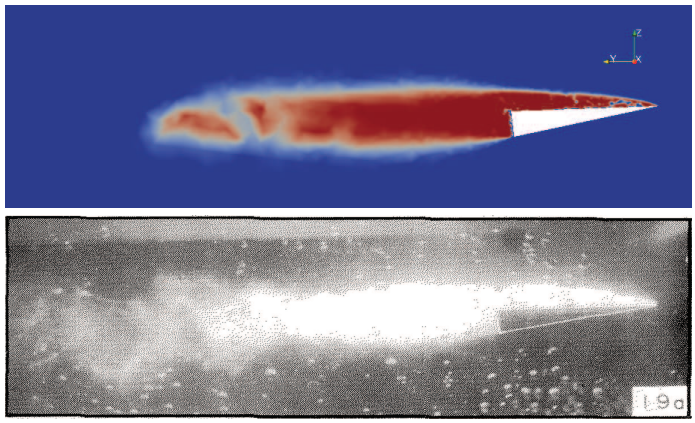

(b) $\sigma_V = 0.284$ CFD

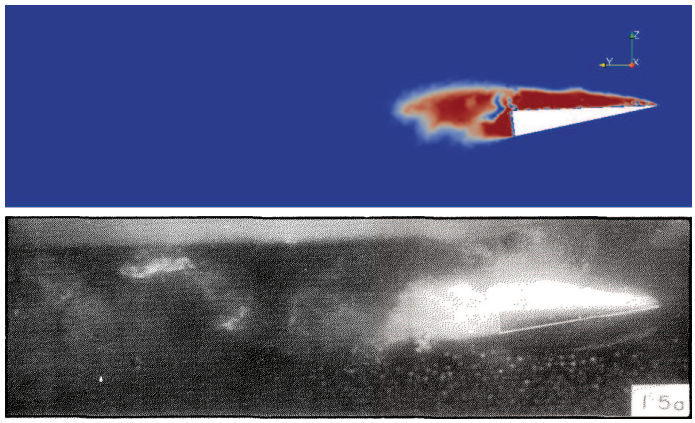

(c) $\sigma_V = 0.534$ CFD

Figure 17: Comparison of the cavity shape predicted by the proposed numerical model and the exprimental observation. Flat plate at $\alpha = 7\ deg$. $\tau = 20.68$

The particular shape of the hydrofoil creates a very complex flow pattern which results in a highly unstable flow over the entire σ_V range. A good agreement is found with experiments also for this profile shape: the relative error with respect to measured values is generally below 5%, slightly increasing for higher cavitation indexes, where flow instabilities become more relevant. Grid FP2 shows the best overall accuracy in the prediction of the drag force and in general no significant improvements are brought in by more refined grids.

The camber on the face of this hydrofoil geometry produces lift also at $\alpha = 0\ deg$. The numerical prediction of c_L are compared with experiments in figure 19. It can be observed that the URANS solver predicts a negative averaged value of lift in the whole σ_V range, while positive values have been measured at higher cavitation indexes in the cavitation tunnel. At these flow conditions the cavity shape instabilities can drastically affect the flow pattern in terms of pressure and velocity fields close to the hydrofoil surface. The standard deviation of the numerical drag signal is twice as large as the average value at the highest σ_V.

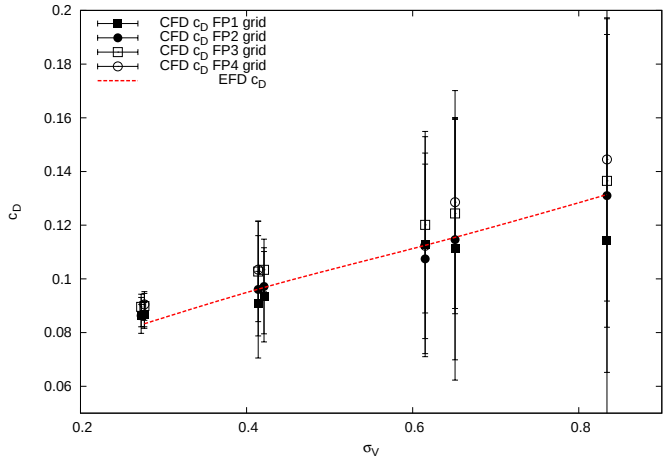

Figure 18: Drag Coefficient predictions at different cavitation indexes σ_v. Dots: numerical results obtained with different mesh resolutions; curve experimental measurements. Circular Arc geomtery at $Re = 6.19E5$, $\alpha = 0\ deg$.

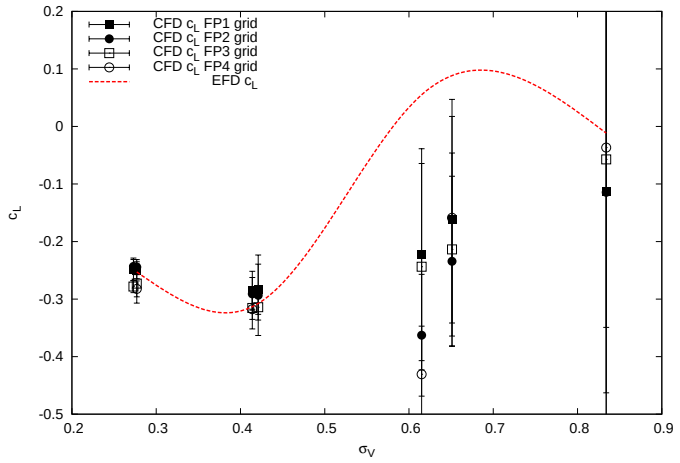

Figure 19: Lift Coefficient predictions at different cavitation indexes σ_v. Dots: numerical results obtained with different mesh resolutions; curve experimental measurements . Circular Arc geomtery at $Re = 6.19E5$, $\alpha = 0\ deg$.

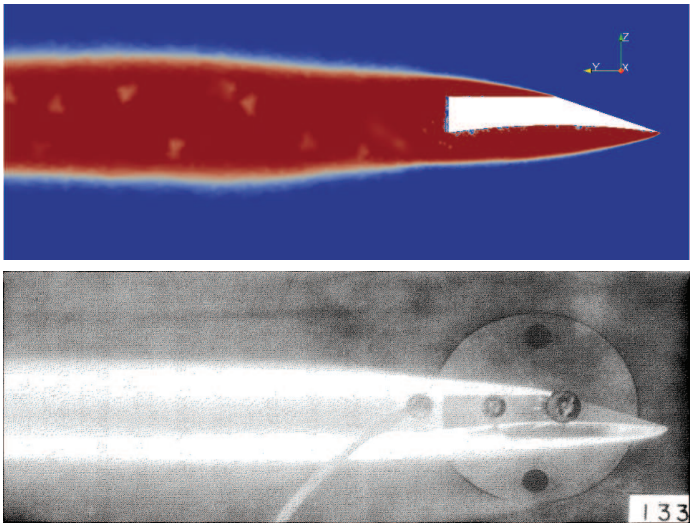

(a) $\sigma_V = 0.277$. Top pannel CFD, bottom pannel EFD

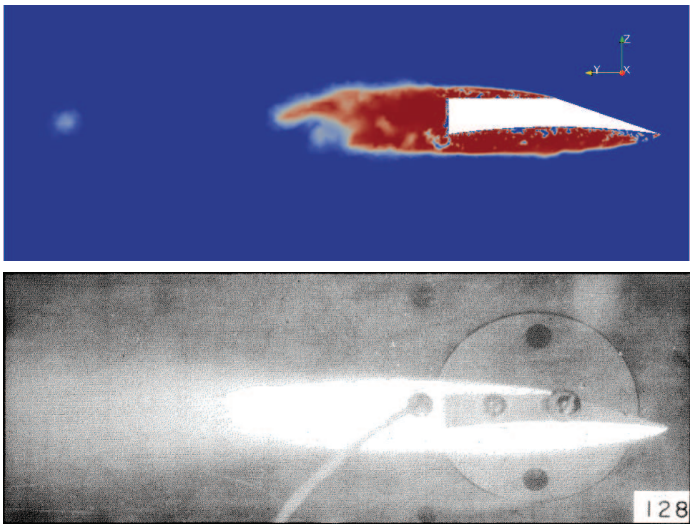

(b) $\sigma_V = 0.421$ Top pannel CFD, bottom pannel EFD

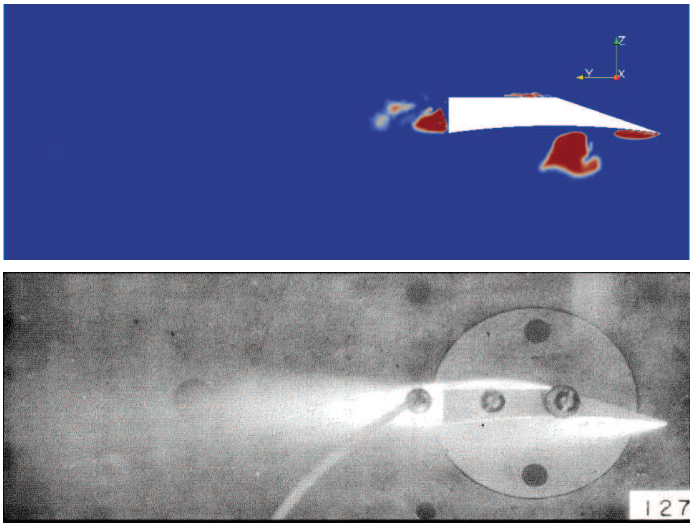

(c) $\sigma_V = 0.834$ Top pannel CFD, bottom pannel EFD

Figure 20: Comparison of the cavity shape predicted by the proposed numerical model and the exprimental observation. Circular arc profile at $\alpha = 0$ *deg*. $\tau = 30$

This adds some concerns on the accuracy of the experimental measurements, since no information in given about the unsteady nature of the measured forces. Nevertheless, numerical prediction of lift for $\sigma_V = 0.273$, $\sigma_V = 0.277$, $\sigma_V = 0.414$ and $\sigma_V = 0.421$ are generally characterized by a relative error of approximately 5% for the four grids used in this study.

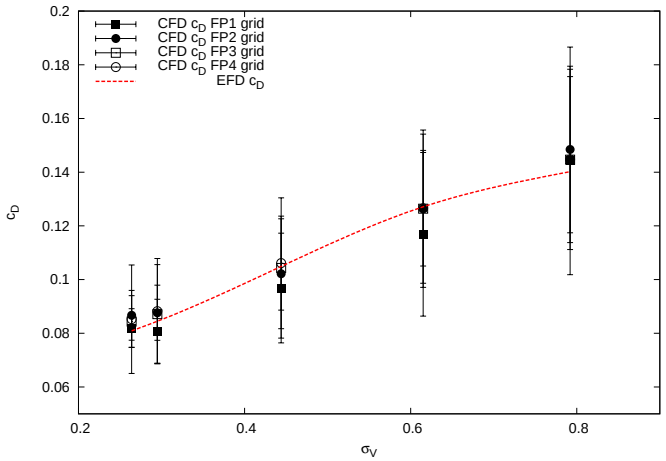

Figure 21: Drag Coefficient predictions at different cavitation indexes σ_v. Dots: numerical results obtained with different mesh resolutions; curve experimental measurements. Circular Arc geomtery at $Re = 6.19E5$, $\alpha = 10$ *deg*.

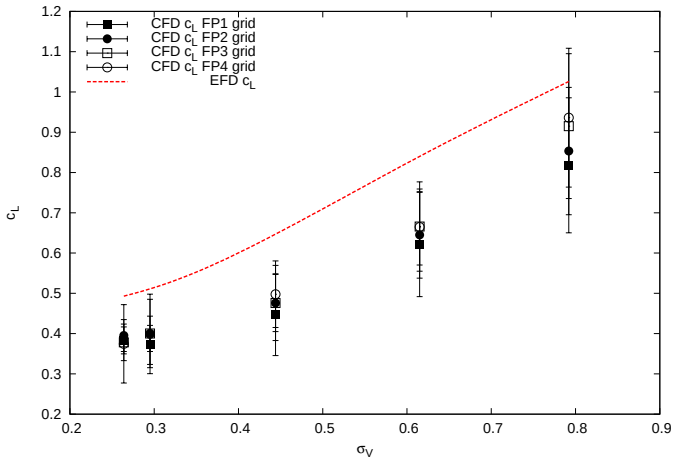

Figure 22: Lift Coefficient predictions at different cavitation indexes σ_v. Dots: numerical results obtained with different mesh resolutions; curve experimental measurements . Circular Arc geomtery at $Re = 6.19E5$, $\alpha = 10$ *deg*.

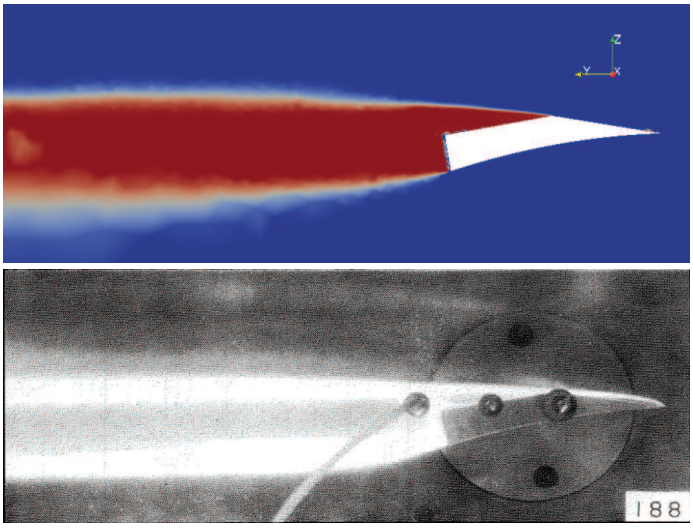

(a) $\sigma_V = 0.264$ Top pannel CFD, bottom pannel EFD

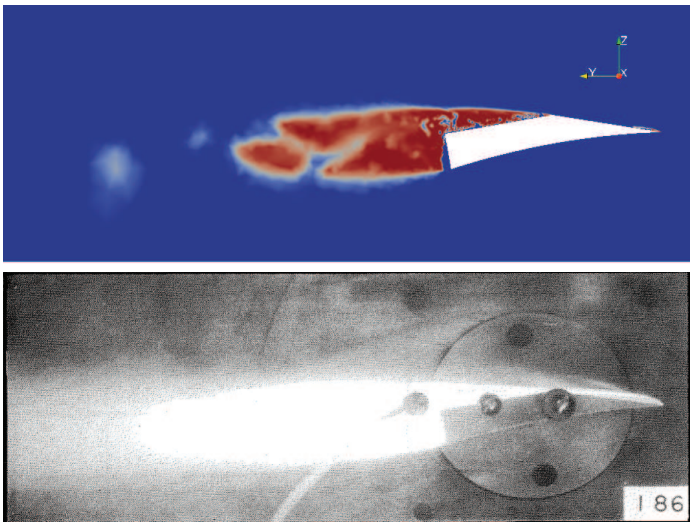

(b) $\sigma_V = 0.444$ Top pannel CFD, bottom pannel EFD

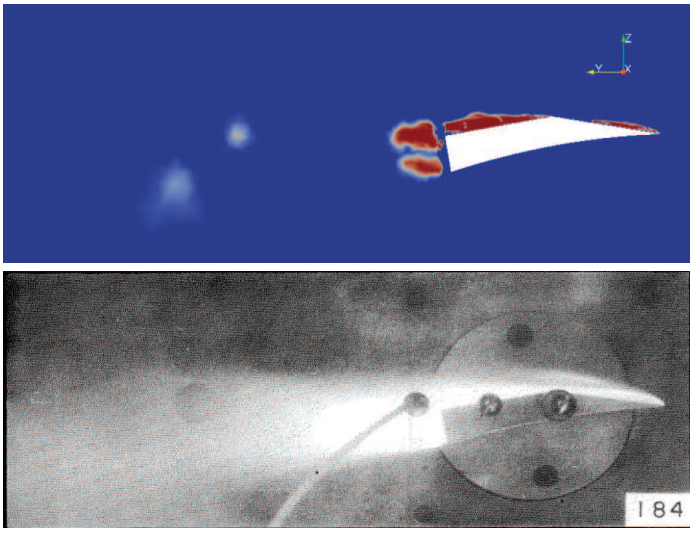

(c) $\sigma_V = 0.792$ Top pannel CFD, bottom pannel EFD

Figure 23: Comparison of the cavity shape predicted by the proposed numerical model and the exprimental observation. Circular arc at $\alpha = 10\ deg$. $\tau = 30$

Figure 20 shows the comparison between the experimental and the numerical cavity shape for the circular arc geometry at $\alpha = 0\ deg$. Figures 20(a) and 20(b) show results at $\sigma_V = 0.277$ and $\sigma_V = 0.421$ respectively. A supercavitating flow regime is predicted at these operating conditions and the numerical results agree with experiments both in terms of cavity length and thickness.
Figure 20(c) confirms what presented in figure 19: the URANS solution shows larger differences with the experiments. The CFD predicts a partial cavitation on the pressure side close to the leading edge, while the cavity has vanished in the suction side. At the same $\sigma_V = 0.834$ experiments show a supercavity covering both the suction and the pressure side.
The circular arc geometry has been simulated at an angle of attack $\alpha = 10\ deg$: global results are shown in figures 21 and 22 for c_D and c_L respectively. In this particular flow condition the FP1 grid show the largest deviation (underestimation) on the drag coefficient in almost the entire σ_V range. The high values of standard deviation noticeable in figure 21 indicate that as for $\alpha = 0\ deg$, the flow conditions are strongly unsteady in the whole cavitation index range. The relative error with experiments is generally lower than 8%, having an average value over the σ_V range of 5% for FP1, 3.2% for FP1, 1.9% for FP3, and %2.3 for FP4, hence showing an advantage in terms of accuracy in adopting finer resolution grids.
Figure 22 presents results in terms of lift coefficient. The c_L is underestimated by averagely 20% for all the numerical grids tested in this study. Figure 23 gives an explanation for the discrepancies in the lift force prediction. Experiments show the existence of a cavitation bubble detaching at the leading edge, while the URANS solver predicts the cavity detachment at the sharp edge located at 29.51 *mm* from the leading edge. This is due to an higher pressure field predicted by the CFD solver, which results in a lower lift force. Figure 23 also shows that the length and thickness of the cavity are slightly underpredicted by the URANS solver.

Conclusion

A new simulation framework, specifically designed for the fluid dynamic analysis of 2D hydrofoils has been described in detail and validated against experimental measurements on two different supercavitating hydrofoils. The computational tool is fully automated and it was developed with the final aim to be included into a shape optimization procedure.
The simulation framework consists of three main modules: the *preprocessing* tool which performs the numerical grid generation of any type of hydrofoil geometries, the *CFD* package based on the solution of the Navier-Stokes equations and a *post-processing* module, specifically designed to give results in terms of transient-free lift and drag coefficients.
The main advantage of such a framework is the simple interface with external tools for geometry generation (input) and the minimal requirement of input data. The capability of dealing with any type of hydrofoil geometries, building robust hybrid structured/unstructured numerical grids represents the most important step forward towards the reduction of computational times usually required for high fidelity simulations.
The mesh generation is automatically performed in few seconds for different hydrofoil shapes at different angles of attack. The numerical simulation is automatically set-up according to the specific flow regime that has to be predicted. The possibility of tuning the RANS solver according to the specific fluid dynamic problem allows to easily switch from cavitating to non-cavitating flow, in steady or unsteady conditions, with

or without wall functions, using different turbulence models.
The simulation framework has been verified on a series of successively refined grids and validated using two different hydrofoil geometries. The RANS solver has been tested in laminar flow regime without wall functions using an unsteady solver specifically designed for cavitating flows. The multiphase flow has been solved using the well established VOF capturing technique which partially drove the design of the numerical grid.
Two series of tests done in the high speed cavitation tunnel of Caltech on two different 2D super-cavitating hydrofoils have been taken as reference data for validation. Unfortunately no many other experimetnal results on 2D supercavitating hydrofoils are available in addition to these. The numerical predictions in terms of c_D and c_L have been compared with the values measured by Parkin (1956) in a systematic series of simulations which covered two different angles of attack and a wide range of cavitation indexes. Drag coefficient has been accurately predicted both for the wedge and the circular arc geometry at each angle of attack. Numerical results generally showed a relative error with respect to experiments of approximately 5% both for the drag and for the lift coefficient of the wedge hydrofoil. Some discrepancies have been found in the c_L predictions of the circular arc geometry.
An interesting comparison have been made possible by a series of photographs of the cavitating flow shot during the experiments, generally showing a good match between the numerical and the experimental cavity shape.
The presented tools is now mature enough to be incorporated into more complex design by optimization procedure and it is expected to allow for the design of unconventional super-cavitating hydrofoils with reliable and consistent hydrodynamic performance.

References

Acosta, A. J. (1955). A note on partial cavitation of flat plate hydrofoils. Technical Report Tech. Rep. E-19.9, California Institute of Technology Hydrodynamics Lab., Pasedena.

Bonfiglio, L. and Brizzolara, S. (2015). Effect of turbulence models on RANSE predictions of transient flow over blade sections. In *Proceedings of the Workshop on Cavitation and Propeller Performance Fourth International Symposium on Marine Propulsors-smp´15*.

Brizzolara, S. (2015). A New Family of Dual-Mode Super-Cavitating Hydrofoils. In *Proceedings of the Workshop on Cavitation and Propeller Performance Fourth International Symposium on Marine Propulsors-smp´15*.

Campana, E. F., Peri, D., Tahara, Y., and Stern, F. (2006). Shape optimization in ship hydrodynamics using computational fluid dynamics. *Computer Methods in Applied Mechanics and Engineering*, 196:634–651.

Celik, F., Ozden, Y. A., and S.Bal (2014). Numerical Simulation of the Flow around Two-dimensional Partially Cavitating Hydrofoils. *J. Marine Sci. Appl.*, 13:245–254.

Delaunay, B. (1934). Sur la sphere vide. A la mémoire de Georges Voronoi. *Bulletin de l'Academie des Sciences de l'URSS, Classe des sciences mathematiques et naturelles*, 6:793–800.

Fine, N. and Kinnas, S. (1993). A boundary element method for the analysis of the flow around 3-D cavitating hydrofoils. *Journal of Ship Research*, 37:213–224.

Geuzaine, C. and Remacle, J. (2009). Gmsh: a three-dimensional finite element mesh generator with built-in pre- and post-processing facilities. *International Journal for Numerical Methods in Engineering*, 79:1309–1331.

Issa, R. (1985). Solution of the implicitly discretized fluid flow equations by operator splitting. *Journal of Computational Physics*, 62:40–65.

Ji, B., Luo, X. W., Arndt, R. E. A., Peng, X., and Wu, Y. (2015). Large Eddy Simulation and theoretical investigation of the transient cavitating vortical flow structure around a NACA66 hydrofoil. *International Journal of Multiphase Flow*, 68:121–134.

Kalitzin, G., Medic, G., Iaccarino, G., and Durbin, P. A. (2005). Near-wall behavior of RANS turbulence models and implications for wall functions. *Journal of Computational Physics*, 204:265–291.

Kim, Y. G. and Lee, C. S. (1996). Prediction of unsteady performance of marine propellers with cavitation using surface-panel method. In *Proceedings of 21th Symposium on Naval Hydrodynamics, Trondheim, Norway*.

Kinnas, S. and Fine, N. (1991). Non-linear analysis of the flow around partially or super-cavitating hydrofoils by a potential based panel method. In *Symposium on Boundary Integral Methods Theory and Applications Springer Verlag*, pages 289–300.

Kinnas, S. and Fine, N. (1992). A nonlinear boundary element method for the analysis of unsteady propeller sheet cavitation. In *Nineteenth Symposium on Naval Hydrodynamics*, pages 717–737.

Kinnas, S. A., Mishima, S., and Brewer, W. H. (1994). Non linear Analysis of Viscous Flow Around Cavitating Hydrofoils. In *Twentieth Symposium on Naval Hydrodynamics*.

Kissling, K., Springer, J., Jasak, H., Shuütz, S., Urban, K., and Piesche, M. (2010). A coupled pressure based solution algorithm based on the volume of fluid approach for two or more immiscible fluids. In *V European Conference on Computational Fluid Dynamics, Lisbon, Portugal*.

Knapp, R. T., Levy, J., O'Neill, J. P., and Brown, F. B. (1948). The Hydrodynamic Laboratory of the Californian Institute of Technology. *Trans. ASME*, 70:437–457.

Knopp, T. (2006). ON GRID-INDEPENDENCE OF RANS PREDICTIONS FOR AERODYNAMIC FLOWS USING MODEL-CONSISTENT UNIVERSAL WALL-FUNCTIONS. In *European Conference on Computational Fluid Dynamics, ECCOMAS CFD 2006*.

Knopp, T., Alrutz, T., and Schwamborn, D. (2006). A grid and flow adaptive wall-function method for rans turbulence modelling. *Journal of Computational Physics*, 220:19–40.

Launder, B. and Spalding, B. (1972). *Mathematical Models of Turbulence*. New York: Academic Press.

Lord Rayleigh, O. M. F. R. S. (1917). VIII. On the pressure developed in a liquid during the collapse of a spherical cavity. *Philosophical Magazine Series 6*, 34:200:94–98.

OpenFOAM Foundation (2011-2014). OpenFOAM User Manual.

Parkin, B. R. (1956). Experiments on circular arc and flat plate hydrofoils in noncavitating and full cavity flows. Technical Report Report No. 47-6, California Institute of Technology Hydrodynamics Lab., Pasedena.

Piquet, J. (1999). *Turbulent Flows*. Springer.

Sauer, J. and Scnherr, G. H. (2001). Development of a New Cavitation Model based on Bubble Dynamics. *Journal of Applied Mathematics & Mechanics - Zeitschrift für Angewandte Mathematik und Mechanik*, 81:561–562.

Sjunnesson, A., Nelsson, C., and Max, E. (1991). LDA measurements of velocities and turbulence in a bluff body stabilized flame. *Laser Anemometry*, 3:83–90.

Tulin, M. P. (1953). Steady two-dimensional cavity flows about slender bodies. Technical Report Technical Report N.834, DTMB.

Uhlman, J. J. S. (1987). The surface singularity method applied to partially cavitating hydrofoils. *Journal of Ship Research*, 31(2):107–124.

Vernengo, G. and Brizzolara, S. (2015). Resistance and Seakeeping Optimization of a Fast Multihull Passenger Ferry. *International Journal of Offshore and Polar Engineering*, 25(1):26–34.

Young, Y. L. and Kinnas, S. A. (2001). A BEM for the Prediction of Unsteady Midchord Face and/or Back Propeller Cavitation. *Journal of Fluids Engineering*, 123:311–319.

Acknowledgement

The development of the simulation framework described in this paper has been constantly supported and advised by Dr. Stefano Brizzolara, Director of the MIT i-Ship lab.
This work has been developed in the context of the DARPA Project HR0011-14-1-0060.

Biography

Luca Bonfiglio : Luca earned his Master of Science from University of Genoa in 2009. After working on the design of fast patrol crafts for an engineering firm in Italy, he worked as an energy superintendent for a French shipping company. In 2011 he started his PhD program at University of Genoa, where he worked with open-source RANSE solvers, specializing in the seakeeping of innovative SWATH vessels. During the last period of his PhD he designed a simulation framework for the solution of hydrofoil hydrodynamics. After earning the PhD degree he started working at the MIT i-Ship Design Lab as a Post-doctoral Associate where he continued the development of his simulation framework.